Scattering Manipulation for Conformal Coding Metasurfaces Based on a Graphene-Assembled Film

Zhi-Feng Li, Rong-Guo Song, *Member, IEEE*, Hao-Ran Zu, *Member, IEEE*, Yu Zhou, Yi-Tong Xin, Jian-Nan Guo, Rui-Xue Zhang, and Da-Ping He

***Abstract*—Electromagnetic (EM) scattering modulation on arbitrarily shaped platforms is crucial for practical communication systems. Metasurfaces offer significant potential because of their strong EM wave control capabilities. This article presents a conformal array scattering theory (CAST) for precise beam manipulation on 2-D conformal coding metasurfaces (CCMs). Due to the incident wave angle and the curved surface shape, elements exist scattering shadow regions. Therefore, we investigate the spatial direction and distribution of the scattering fields from subarrays composed of 1-bit elements, while analyzing the formation mechanism of the scattering shadow regions. By incorporating wave path and reflection phase changes induced by structural bending, we establish an accurate theoretical model to compute the far-field scattering pattern of CCMs. To validate the approach, a CCM based on a graphene-assembled film (GAF) with ultrahigh conductivity and excellent mechanical properties such as flexibility and lightweight is used to fabricate the designs. The flexible GAF can provide additional spatial freedom through structural bending, enabling curvature-based scattered beam manipulation without requiring other active devices. Theoretical analysis, simulations, and measurements show good agreement, demonstrating the potential of this method for designing conformal arrays for various curved platforms.**

***Index Terms*—Beam manipulation, conformal array scattering theory (CAST), flexibility, graphene-assembled film (GAF), lightweight, metasurface.**

I. Introduction

METAMATERIALS, as artificially engineered structures, exhibit numerous novel electromagnetic (EM) phenomena, such as wavefront manipulation [1], [2], [3], [4], [5], polarization conversion [6], [7], [8], radar cross section reduction [9], [10], [11], and cloaking [12], [13]. With the introduction of generalized Snell's laws [14], metasurfaces have experienced explorative development, and various interesting devices have been developed in the microwave and optical domains. Cui et al. [15] proposed the concept of coding metamaterials using planar array theory. The element reflection phase can be quantized into binary codes, for example, the 1-bit code "0/1" indicates that the element can have two different reflection coefficients. Planar metasurfaces can incorporate tunable materials or components, such as diodes [16], [17], [18], vanadium dioxide [19], and phase-change materials [20], [21], to realize active control of EM behaviors in dynamic fashions.

Despite the progress discussed above toward planar devices, conformal techniques have attracted much attention. The design of conformal coding metasurfaces (CCMs) requires establishing the relationship between the wavefront and the curved surface. In microwave and terahertz frequencies, the EM properties and modeling methods for CCMs are discussed and researched [22], [23], [24], [25], [26]. For example, Fan et al. [27] applied the generalized Snell law to the design of conformal metasurfaces, achieving multiangle efficient microwave scattering enhancement. Li et al. [28] proposed a general theoretical strategy for projecting curved surfaces onto a reference plane, enabling multifunctional wavefront control on curved platforms. Zhou et al. [29] extended the array theory to design 2-D curved coding metasurfaces, achieving arbitrary wavefront control. Although several methods have been proposed for the scattering manipulation of CCMs, they often simplify the theoretical computational models, leaving some problems unresolved. For example, the designed elements must remain insensitive to incident angles to adapt to incident EM waves from different directions [30]. Consequently, the variations in the reflection phase and amplitude of the elements are often ignored. In particular, general array theory typically employs only the point source model (PSM) [31], [32] for array synthesis, which does not account for scattering shadow regions. These issues affect the accuracy of far-field scattering calculations and hinder the optimization of conformal array layouts [33]. Therefore, it is essential to explore a new approach to achieve reliable scattered beam manipulation on CCMs.

Furthermore, most CCMs reported so far have fixed curvatures and complex structures, lacking the flexibility required for applications in modern curved surface systems [34]. This limitation arises, in part, because dielectric substrates are often too thick to bend easily. In addition, incorporating numerous PIN diodes in reconfigurable CCMs restricts structural flexibility and increases the total weight of the system [35], [36]. Most notably, CCMs extensively use copper as

Received 11 December 2024; revised 19 March 2025; accepted 31 March 2025. Date of publication 14 April 2025; date of current version 6 August 2025. This work was supported by the National Natural Science Foundation of China (NSFC) under Grant 62401413. *(Zhi-Feng Li and Rong-Guo Song contributed equally to this work.) (Corresponding author: Hao-Ran Zu.)*

Zhi-Feng Li and Hao-Ran Zu are with the School of Information Engineering, Wuhan University of Technology, Wuhan 430070, China, and also with Hubei Engineering Research Center of RF-Microwave Technology and Application, Wuhan University of Technology, Wuhan 430070, China (e-mail: zuhr@whut.edu.cn).

Rong-Guo Song, Yu Zhou, Yi-Tong Xin, Jian-Nan Guo, Rui-Xue Zhang, and Da-Ping He are with Hubei Engineering Research Center of RF-Microwave Technology and Application, Wuhan University of Technology, Wuhan 430070, China.

Digital Object Identifier 10.1109/TAP.2025.3558585

the metal pattern layer and ground plane. However, copper foils are prone to deformation or cracking under long-term bending, making them unsuitable for conformal applications [37]. Simultaneously, the high density of metallic materials increases the overall weight of the system, and their environmental durability tends to be inadequate. Nowadays, graphene has become a superior alternative to conventional metallic materials, offering significant advantages in flexibility, reduced weight, corrosion resistance, and thermal conductivity [38], [39], [40]. In our previous work, a graphene-assembled film (GAF) with a conductivity of 10^6 S/m and lightweight has been effectively used in the design of various flexible RF microwave devices, including RFID tags [41], filters [42], FSSs [43], and wearable antennas [44]. These findings suggest that the GAF, as a novel flexible carbon-based conductive material, holds significant promise for the design of CCMs. Importantly, flexible CCMs with adjustable curvature provide additional spatial degrees of freedom [45], [46], [47], making it possible to achieve dynamic beam scanning through structural bending if the scattering field of the CCM can be accurately predicted.

In this article, a novel design methodology called conformal array scattering theory (CAST) for the CCM is proposed and demonstrated. Compared with the PSM method, CAST accounts for the variation of scattering characteristics with the spatial positions of elements. The accuracy of CAST is beneficial for obtaining the desired CCM layout when combined with optimization algorithms. For CCMs with central angles of $[90°, 120°, 150°]$, the optimized subarray layout achieves single-beam and double-beam scattering. To verify the theory, a GAF-based CCM was designed, fabricated, and experimentally tested. The CCM is fabricated using the flexible GAF, facilitating conformal design and adjustable curvature. In experimental verification, the CCM is placed on arc-shaped structures with central angles of $[90°, 100°, 110°]$, achieving 2-D beam scanning using the spatial freedom provided by different curvatures. The experimental results agree well with the simulations and theoretical predictions, demonstrating the precision of the CAST method in manipulating the scattering field on curved platforms.

This article is organized as follows. In Section II, the element design and the CAST method are introduced. Section III establishes the optimization algorithm for the beam modulation of CCMs, and the results of CAST and full-wave simulation are also discussed. In Section IV, a prototype of the proposed CCM is fabricated, assembled, and tested, and the measurement results of the prototype are discussed. Section V concludes the work.

II. Conformal Array Scattering Theory

A. Element Design and Analysis

The schematic of the metasurface element is shown in Fig. 1(a). As can be seen, the I-shaped GAF pattern is used as the top layer and a continuous GAF acts as the bottom layer, in which the GAF layers exhibit an ultrahigh conductivity of 2.58×10^6 S/m and thickness of 0.025 mm. The middle layer is composed of expanded polyethylene (EPE) with a thickness

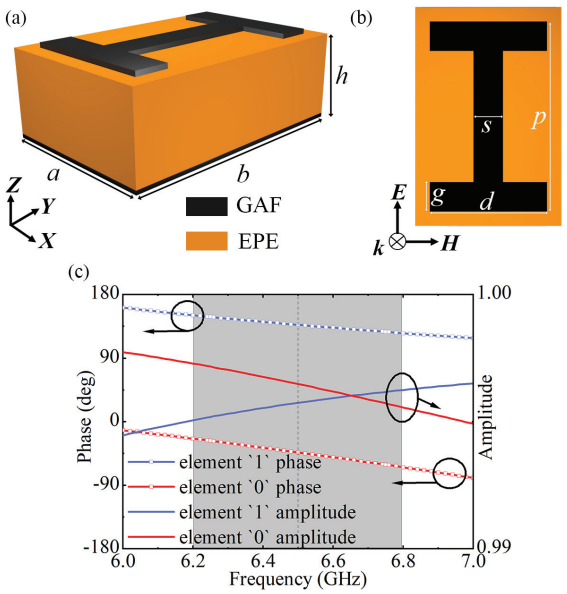

Fig. 1. (a) 3-D schematic of the metasurface element. (b) Top view of the I-shaped GAF pattern with geometric parameters s, p, g, and d. (c) Reflection amplitude and phase responses of the 1-bit coding elements.

of $h = 5$ mm, which is a low-loss microwave foam with ε_r and $\tan\delta$ of 1.05 and 0.0005, respectively. Fig. 1(b) shows the detailed physical geometry of the I-shaped pattern on the top layer. It has a period of $a = 10$ mm and $b = 15$ mm, and other geometric parameters are optimized as $g = 2$ mm, $s = 2$ mm, $d = 8$ mm, and $p = 13$ mm. In particular, the side lengths of the metasurface element are not equal ($a \neq b$). The short side length a implies that the total length of the CCM is reduced along the x-direction. This reduction is beneficial in minimizing the drastic changes in the wave path caused by the bending of the structures.

To investigate the reflection characteristics of the designed element, full-wave simulations are performed using the commercial software CST Microwave Studio (CST). The element is illuminated by a TE-polarized wave with the electric field along the y-direction. Periodic boundary conditions are set for the x- and y-directions and an open boundary for the z-direction. Fig. 1(c) depicts the reflection magnitude and phase responses of the elements as p increases from 9 to 13 mm, corresponding to states "0" and "1," respectively. The gray areas indicate the operating bandwidth (6.2–6.8 GHz), within which the phase difference between the element "0" and "1" is $180° \pm 10°$. It can be observed that a 180° phase difference is achieved at the center frequency of 6.5 GHz (dotted line marks). Due to the continuous GAF on the bottom layer, the entire structure is perfectly reflective of the incident wave. The reflection amplitude remains above 0.99 within the frequency band, demonstrating the potential of the GAF for high-efficiency wavefront manipulation. For a 1-bit planar metasurface, scattered beams are typically controlled using array pattern synthesis (APS) theory, which relies on the reflection phase of the elements. However, this approach is unsuitable for conformal targets as the oblique incidence caused by structural bending affects the reflective properties

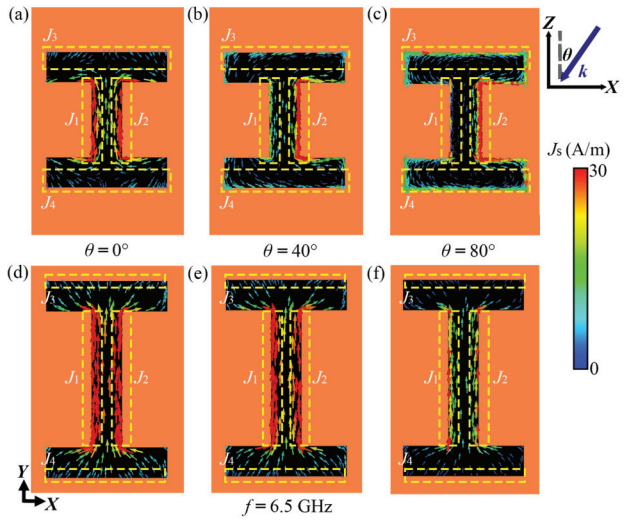

Fig. 2. Surface current distributions on the metasurface elements at 6.5 GHz at different angles of oblique incidence. (a)–c) Current distributions of the element (p = 9 mm). (d)–(f) Current distributions of the element (p = 13 mm). The yellow dashed lines mark the different surface current distribution regions.

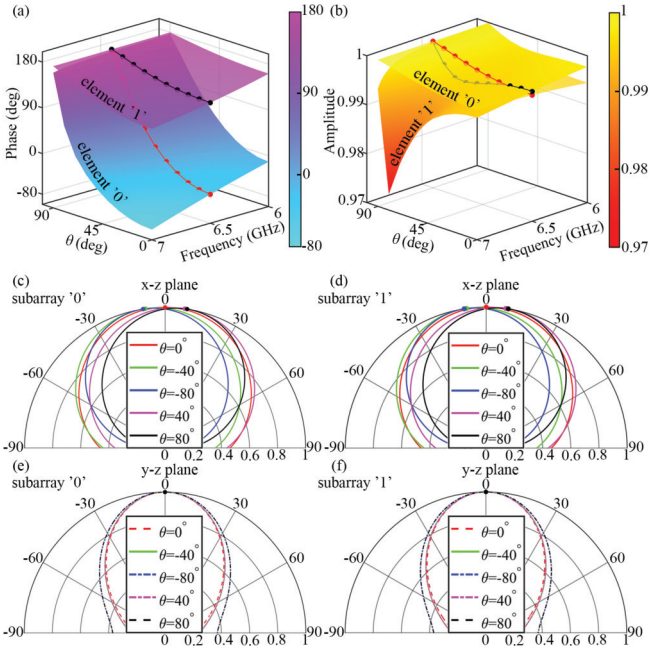

Fig. 3. (a) and (b) Phase and amplitude of the element at different incident angles θ within the frequency range of 6–7 GHz. (c)–(f) Simulated normalized scattering patterns of subarrays "0" and "1" at 6.5 GHz in both xz and yz planes. The TE-polarized wave is incident from −80° to 80° in the xz plane.

of the elements. The amplitude and phase of the reflection from different elements on a CCM can vary significantly. Even for isotropic elements, oblique incidence with different polarizations leads to distinct EM responses [48]. As shown in Fig. 2(a)–(f), for TE-polarized waves incident at angles $\theta = [0°, 40°, 80°]$ in the xz plane, the surface current distributions vary with oblique incidence. At $\theta = 0°$ [Fig. 2(a)], surface currents J_1 and J_2 are symmetrically distributed on the I-shaped element (p = 9 mm) at 6.5 GHz, indicating an EM mode. As the angle of incidence increases to $\theta = 40°$ [Fig. 2(b)], this symmetry is disrupted; J_1 weakens, while J_2 intensifies, and the transverse currents J_3 and J_4 begin to strengthen. At $\theta = 80°$ [Fig. 2(c)], due to the large angle of oblique incidence with a transverse wave vector, the surface current distribution changes dramatically, and significant transverse currents J_3 and J_4 appear on the element, indicating the formation of the surface wave [49], [50]. Consequently, the initial EM mode is completely disrupted, resulting in unstable phase responses of the reflected wave. For the element with p = 13 mm [Fig. 2(e) and (f)], the surface current distribution remains unchanged with increasing oblique incidence. The well-symmetrical distribution of J_1 and J_2 persists even at θ = 80°. The increased distance between the upper and lower arms weakens the EM mode in the "concave" region, minimizing transverse currents J_3 and J_4. Therefore, the uniform surface current distribution makes the reflection phase of the element insensitive to oblique incidence. Note that as the parameter p increases, if the spacing between the upper and lower arms of adjacent elements becomes very small, significant interelement coupling may occur. Excessive coupling may lead to additional surface wave interference. In our design (p = 13 mm), the currents J_3 and J_4 remain consistently low, thereby preventing the formation of a continuous coupled current distribution.

Fig. 3(a) and (b) illustrates the variation in the reflection characteristics of the "0" and "1" elements as the incident angle θ and frequency f. In Fig. 3(a), it can be observed that the phase of element "0" increases significantly with the incident angle θ, exceeding a 180° change within the bandwidth. On the other hand, the phase of element "1" remains relatively stable. The above phase variations of both elements "0" and "1" are consistent with their surface current analysis shown in Fig. 2. Due to the highly efficient reflection properties of the GAF bottom layer for incident wave, the amplitude variation of both element "0" and element "1" with the incident angle θ is less than 0.03, as shown in Fig. 3(b). The amplitude of element "1" shows a slight decrease at 7 GHz with increasing incident angle θ, while the amplitude of element "0" remains above 0.99. Here, at 6.5 GHz, the red and black dotted curves, respectively, mark the phase and amplitude changes of elements "0" and "1" with varying incident angles θ. For any frequency f, when a TE-polarized wave is incident at an angle θ, the reflection phase and amplitude of the element can be defined as follows:

$$\begin{cases} \phi_0(\theta, f) = \mathcal{F}_{\phi_0}(\theta, f), & \text{(Phase for state '0')} \\ A_0(\theta, f) = \mathcal{F}_{A_0}(\theta, f), & \text{(Amplitude for state '0')} \\ \phi_1(\theta, f) = \mathcal{F}_{\phi_1}(\theta, f), & \text{(Phase for state '1')} \\ A_1(\theta, f) = \mathcal{F}_{A_1}(\theta, f), & \text{(Amplitude for state '1')} \ . \end{cases} \tag{1}$$

The function mapping operator $\mathcal{F}$ defines the dependency of phase and amplitude on the incident angle θ and frequency f for both states. The specific functional form can be determined using the polynomial fitting tool in MATLAB.

To better evaluate the variation in the scattering field of the elements, a subarray is formed by arranging 2 × 1 elements ("0" or "1") along the y-direction. For an incident wave angle ranging from −80° to 80°, the transient solver of CST is

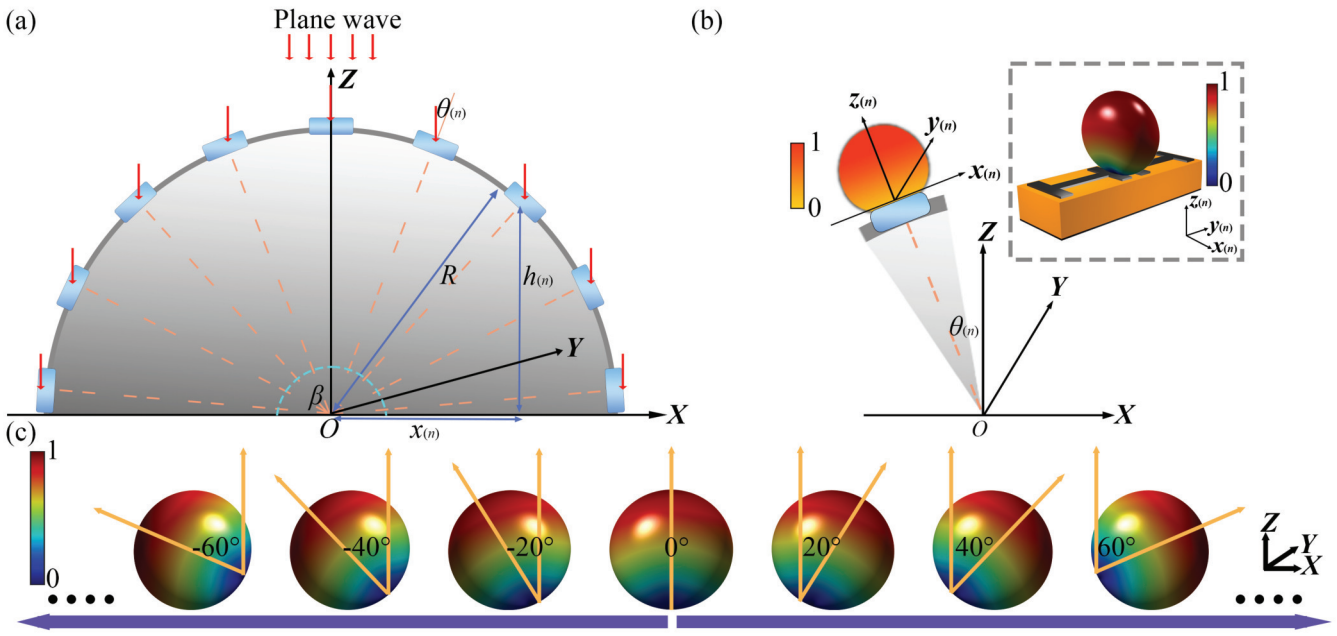

Fig. 4. (a) Schematic of an EM wave incident on the CCM, with subarrays arranged at equal intervals along the CCM profile. (b) Distribution of the scattering patterns of the nth subarray on the CCM; the inset shows the subarray structure with its normalized scattering field. (c) Diagram of the variation of the scattering patterns with $\theta_{(n)}$ in the GCS.

employed to simulate the scattering field of the subarrays. Due to the oblique incidence of TE-polarized wave in the xz plane, the scattering patterns of the subarray are deflected with the incident angle θ, as shown in Fig. 3(c) and (d). The different colored dots represent the normalized maximum values of the scattering patterns. It can be observed that the scattering patterns of both subarrays state "0" and "1" exhibit similar angle deflections. At oblique incidence angles of $\pm 40°$ and $\pm 80°$, the deflection angles are approximately $\pm 6.12°$ and $\pm 6.14°$, respectively. For the yz plane shown in Fig. 3(e) and (f), the scattering pattern of the subarray is not affected by the oblique incidence, maintaining its directionality near 0°. Overall, the scattering patterns of the subarray exhibit only slight deflection with the incident angle. Assuming that all the scattering patterns remain in the forward direction (perpendicular to the element surface), it can be expressed as follows:

$$\begin{cases} P_0^{\theta}(\theta_\perp, \varphi_\perp) \approx P_0^{\theta=0}(\theta_\perp, \varphi_\perp), & \text{(pattern '0')} \\ P_1^{\theta}(\theta_\perp, \varphi_\perp) \approx P_1^{\theta=0}(\theta_\perp, \varphi_\perp), & \text{(pattern '1')} \end{cases} \tag{2}$$

where θ represents the angle of incidence of the oblique. The center of the subarray is defined as the origin of the polar coordinate system, the vertical direction (z-axis) corresponds to $\theta_\perp = 0°$, and the horizontal direction (x-axis) corresponds to $\varphi_\perp = 0°$. Since the scattering patterns "0" and "1" are very similar, $P_0^{\theta}(\theta_\perp, \varphi_\perp)$ and $P_1^{\theta}(\theta_\perp, \varphi_\perp)$ can be considered equal and rewritten as $P^{\theta}(\theta_\perp, \varphi_\perp)$, indicating the scattering field profile. The slight influence of oblique incidence and frequency offset on the scattering pattern can be ignored, thus (2) can be modified as

$$P^{\theta}(\theta_\perp, \varphi_\perp) = P^{\theta=0}(\theta_\perp, \varphi_\perp) \tag{3}$$

where $P^{\theta=0}(\theta_\perp, \varphi_\perp)$ can be obtained from CST. Combining with (1)–(3), the total scattering pattern of the subarray at the frequency f and incident angle θ can be written as

$$F_i^{\theta}(\theta_\perp, \varphi_\perp) = P^{\theta=0}(\theta_\perp, \varphi_\perp) \cdot A_i(\theta, f) \cdot \exp\left[-j\phi_i(\theta, f)\right] \tag{4}$$

where i represents the subarray states "0 "or "1."

B. CAST Method

Fig. 4(a) shows a configuration of the CCM, where the subarrays are arranged at equal intervals of period a along the CCM profile. The uniform plane wave along the Z-axis incident on the subarrays at an angle of $\theta_{(n)}$ relative to the normal in the radial direction of the CCM. Assuming that the period a of each subarray is equal to its arc length dl, the corresponding central angle $\alpha = dl/R$, where R is the radius of curvature (ROC) of the CCM. Using the center of the subarrays as reference points, the $\theta_{(n)}$ of the nth element can be rewritten as

$$\theta_{(n)} = \alpha n - (\beta + \alpha)/2 \tag{5}$$

where the OZ-axis is defined as the origin at 0°. β represents the central angle of the CCM, which is the ratio of the arc length to the ROC. For a planar surface, β is zero. For the same arc length, a smaller β indicates less bending, while a larger β indicates more curvature. In addition, the spatial positions $x_{(n)}$ and $h_{(n)}$ define the coordinates of the subarrays. The position of the nth subarray should satisfy

$$x_{(n)} = R \sin\theta_{(n)}, \quad h_{(n)} = R \cdot \left[\cos\theta_{(n)} - \cos(\beta/2)\right]. \tag{6}$$

Due to the CCM being composed of m-rows subarrays with period $2b$ along the y-axis direction, the distance $y_{(m)}$ from the mth subarray to origin is $2b(m - 0.5)$, depending on

the selection of the reference point. Based on this coordinate information, we can calculate the wave path difference $\phi'_{(m,n)}$ of each subarray. Using the bottom plane of the conformal structure as the zero phase reference plane, the phase difference can be derived as

$$\phi'_{(m,n)} = 2k_0 h_{(n)} + k_0 \sin\theta \cdot \left[\cos\varphi \cdot x_{(n)} + \sin\varphi \cdot y_{(m)}\right] \tag{7}$$

where θ and φ are the elevation and azimuth angles of an arbitrary direction, respectively, and k_0 is the wave vector in free space. Then, we should establish the relation between the scattering field of the nth subarray and the conformal structure. As shown in Fig. 4(b), the inset shows the structure of the subarray with its normalized scattering field. According to (4), the scattering pattern of the nth subarray can be expressed as $F_i^{\theta_{(n)}}(\theta_\perp, \varphi_\perp)$, which is related to the radial direction of the CCM (orange dashed line).

In general, conformal APS (CAPS) is based on the global coordinate system (GCS) of the conformal structure, while $F_i^{\theta_{(n)}}(\theta_\perp, \varphi_\perp)$ is established in the local coordinate system (LCS) of the subarrays. The components of the scattering pattern in the LCS can be expressed as

$$\begin{bmatrix} F^i_{x(n)} \\ F^i_{y(n)} \\ F^i_{z(n)} \end{bmatrix} = F_i^{\theta_{(n)}}(\theta_\perp, \varphi_\perp) \begin{bmatrix} \sin\theta_\perp \cos\varphi_\perp \\ \sin\theta_\perp \sin\varphi_\perp \\ \cos\theta_\perp \end{bmatrix} \tag{8}$$

where $F^i_{x(n)}$, $F^i_{y(n)}$, and $F^i_{z(n)}$ are the scattering components of the nth subarray i in the LCS $[x_{(n)}, y_{(n)}, z_{(n)}]$. Since the LCS is only associated with $\theta_{(n)}$ in the GCS, the corresponding scattering components in the GCS can be obtained through a single Euler rotation transformation. According to (8), we can obtain

$$\begin{bmatrix} F^i_{X(n)} \\ F^i_{Y(n)} \\ F^i_{Z(n)} \end{bmatrix} = \begin{bmatrix} \cos\theta_{(n)} & 0 & \sin\theta_{(n)} \\ 0 & 1 & 0 \\ -\sin\theta_{(n)} & 0 & \cos\theta_{(n)} \end{bmatrix} \begin{bmatrix} F^i_{x(n)} \\ F^i_{y(n)} \\ F^i_{z(n)} \end{bmatrix} \tag{9}$$

where $F^i_{X(n)}$, $F^i_{Y(n)}$, and $F^i_{Z(n)}$ are the scattering components of the nth subarray i in the GCS $[X, Y, Z]$. Therefore, the scattering pattern of the subarray in the global spherical coordinate system $[\theta, \varphi]$ can be given by

$$\begin{bmatrix} F^i_n(\theta) \\ F^i_n(\varphi) \end{bmatrix} = \begin{bmatrix} \cos\theta\cos\varphi & \cos\theta\sin\varphi & -\sin\theta \\ -\sin\varphi & \cos\varphi & 0 \end{bmatrix} \begin{bmatrix} F^i_{X(n)} \\ F^i_{Y(n)} \\ F^i_{Z(n)} \end{bmatrix}. \tag{10}$$

Equation (8)–(10) actually represent the profile of the scattering pattern of the nth subarray in the LCS. Combining with (4) and (5), corresponding to $P^{\theta=0}(\theta_\perp, \varphi_\perp) \rightarrow P^{\theta_{(n)}}(\theta, \varphi)$. The normalized maximum value of each scattering pattern is determined by $A_i(\theta_{(n)}, f)$. Since the reflection amplitude of the elements is minimally affected by the oblique incidence, it can be approximated as $A_i(\theta_{(n)}, f) = 1$. Therefore, the scattering pattern of the nth subarray i can be expressed as

$$F^i_n(\theta, \varphi) = P^{\theta_{(n)}}(\theta, \varphi) \cdot \exp\left[-j\phi_i\left(\theta_{(n)}, f\right)\right] \tag{11}$$

where $P^{\theta_{(n)}}(\theta, \varphi)$ represents the amplitude distribution of the scattering pattern and $\phi_i(\theta_{(n)}, f)$ represents the phase part.

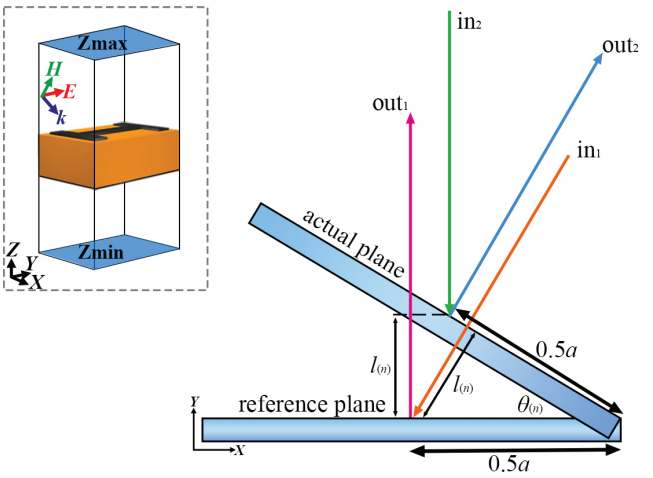

Fig. 5. Schematic of the additional phase correction due to different reference planes. The inset depicts the simulation setup, showing the inclined wave vector $\boldsymbol{k}$ relative to the horizontal plane.

Fig. 4(c) shows the variation of the scattering patterns with $\theta_{(n)}$ in the GCS. Unlike the PSM, the amplitude of the scattered field is not isotropically distributed in space. For example, if the desired deflection angle of the reflected beam is $\theta_0 = 30°$, as $|\theta_{(n)} - \theta_0|$ increases, the scattering contribution of some subarrays to the desired direction will decrease, forming the scattering shadow regions. For the subarrays within $\theta_{(n)} < -60°$, the desired main beam is almost located in the scattering shadow region because $|\theta_{(n)} - \theta_0| > 90°$. Therefore, it is necessary to consider the scattering patterns with different spatial orientations in CAPS.

Based on the above theoretical analysis and combining (7)–(11), the far-field scattering pattern of the $M \times N$ CCMs in arbitrary direction (θ, φ) can be derived as follows:

$$F_{\text{total}}(\theta, \varphi) = \sum_{m=1}^{M}\sum_{n=1}^{N} P^{\theta_{(n)}}(\theta, \varphi) \cdot \exp\left\{-j\left[\phi'_{(m,n)} + \phi_{(m,n)}\left(\theta_{(n)}, f\right) + \phi_{l_{(n)}}\right]\right\} \tag{12}$$

where $\phi_{l_{(n)}}$ represents an additional phase correction term derived from the selection of different reference planes. As illustrated in Fig. 5, to simulate the oblique incidence of waves on metasurfaces, the wave vector $\boldsymbol{k}$ is inclined relative to the horizontal plane (the inset shows the simulation setup). According to (3), it is assumed that the reflected wave is perpendicular to the element surface. When the planar element is used as the reference plane, the wave path can be represented as $\text{in}_1 \rightarrow \text{out}_1$. For the actual reference plane (elements on the CCM), the wave path can be represented as $\text{in}_2 \rightarrow \text{out}_2$. Due to the angle between the two reference planes corresponding to $\theta_{(n)}$, the wave path difference satisfies

$$(\text{in}_1 + \text{out}_1) - (\text{in}_2 + \text{out}_2) = 2l_{(n)} \tag{13}$$

where $l_{(n)} = 0.5a \cdot \sin\theta_{(n)}$, with the center of the different planes selected as the reference point. Consequently, the additional

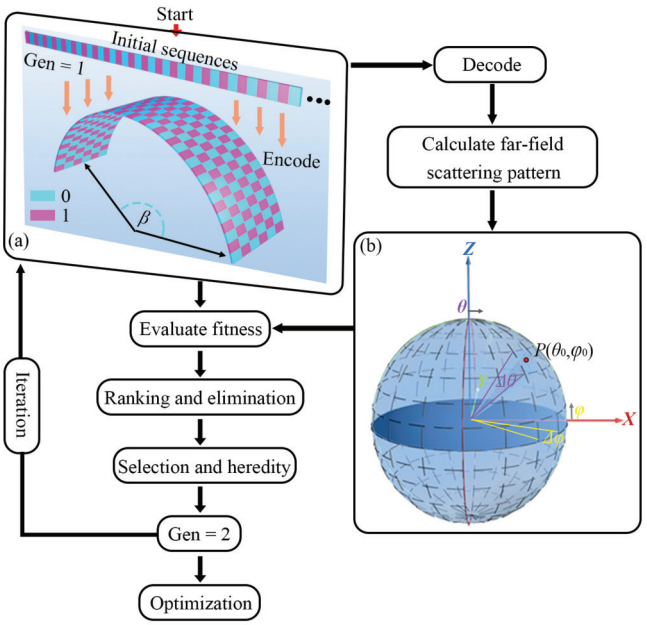

Fig. 6. Flowchart of the optimization algorithm. (a) Initial random $M \times N$ binary sequence is encoded to form a coding matrix. (b) Establishment of the fitness function.

phase can be expressed as

$$\phi_{l_{(n)}} = k_0 a \cdot \sin\theta_{(n)}. \tag{14}$$

III. Beam Optimization and Manipulation

A. Beam Optimization

From Section II-B, it indicates that the scattered beams can be manipulated by encoding the subarrays states "0" or "1." Therefore, the computation of the coding matrix can be formulated as an optimization problem, typically solved using stochastic nonlinear optimization algorithms such as the genetic algorithm (GA) and particle swarm optimization (PSO) [51], [52], [53]. GA, in particular, is a search algorithm based on the principles of natural genetics. Given specific requirements for scattering patterns by metasurfaces, GA can compute the optimal coding matrices. As illustrated in Fig. 6(a), for a CCM with a central angle β, an initial random $M \times N$ binary sequence forms a coding matrix that determines the layout of the subarrays. Each binary digit "0" or "1" represents two possible states of the subarray. In this algorithm, the population is initialized by transforming the coding sequences into chromosomes, which are then evolved in each iteration to find the optimal chromosomes. These optimal chromosomes are subsequently converted into the desired coding matrix. The evolution process includes fitness-based selection, recombination (crossover), offspring mutation, and reinsertion based on offspring fitness, all inspired by natural biological evolution. The evaluation of fitness involves the establishment of optimization objectives. According to (12), the gth generation coding matrix is decoded, and the far-field scattering pattern $F(\theta, \varphi)$ of the CCM can be calculated. As shown in Fig. 6(b), we optimize only the scattering pattern $F(\theta, \varphi)$ in the upper hemisphere, where the ranges of θ and φ are $[0, \pi/2]$ and $[0, 2\pi]$, respectively. The upper hemisphere can be evenly divided, with the polar angle θ divided into p parts and the azimuthal angle φ divided into q parts. We can obtain

$$\theta_i = \frac{2\pi}{p}(i-1), \quad \theta_{i+1} = \frac{2\pi}{p}i, \quad i = 1, 2, \ldots, p \tag{15}$$

$$\varphi_j = \frac{\pi}{2q}(j-1), \quad \varphi_{j+1} = \frac{\pi}{2q}j, \quad j = 1, 2, \ldots, q \tag{16}$$

where the divisions of the polar angle and azimuthal angle can be written as $\Delta\theta_j = [\theta_j, \theta_{j+1}]$ and $\Delta\varphi_i = [\varphi_i, \varphi_{i+1}]$, respectively. Therefore, the upper hemisphere is divided into $D = p \times q$ solid angle regions $\Delta\Omega_{ij}$, the corresponding ranges can be expressed as

$$\Delta\Omega_{ij} = \left\{(\theta, \varphi) | \theta \in \left[\theta_i, \theta_{i+1}\right], \varphi \in \left[\varphi_j, \varphi_{j+1}\right]\right\}. \tag{17}$$

The maximum value of the scattering field $F(\theta, \varphi)$ in each solid angle $\Delta\Omega_{ij}$ can be defined as

$$F_{\max}^{ij} = \max_{\Delta\Omega_{ij}} F(\theta, \varphi). \tag{18}$$

Assuming the desired main beam direction is $P(\theta_0, \varphi_0)$ and $(\theta_0, \varphi_0) \in \Delta\Omega_{i_0 j_0}$. The average scattering intensity in the remaining $(D-1)$ solid angles can be denoted as

$$F_{\text{ave}} = \frac{1}{(D-1)} \sum_{\substack{i=1 \\ i \neq i_0}}^{p} \sum_{\substack{j=1 \\ j \neq j_0}}^{q} F_{\max}^{ij}. \tag{19}$$

The scattering field can be concentrated around the target angles $P(\theta_0, \varphi_0)$ by reducing F_{ave}, thus optimizing the scattering pattern $F(\theta, \varphi)$. To measure the deviation between the optimized result of the gth generation and desired main beam, combining with (19), the final objective function can be given as

$$\begin{aligned} Fitness(g) = w_1 \cdot F_{\text{ave}}\ (g) + w_2 \cdot |\theta_d(g) - \theta_0| \\ + w_3 \cdot |\varphi_d(g) - \varphi_0| \end{aligned} \tag{20}$$

where $\theta_d(g)$ and $\varphi_d(g)$ are the gth optimized results of the main beam direction, corresponding to the global maximum of $F(\theta, \varphi)$. In this article, the weighting coefficients w_1, w_2, and w_3 are set at 100, 1, and 1, respectively. These coefficients balance the contributions of different terms in the objective function and influence the convergence rate. A higher w_1 accelerates the synthesis of the main beam, while w_2, and w_3 are responsible for adjusting the direction of the main beam.

B. Single-Beam and Double-Beam Generation

In this section, single- and double-beam scattering is generated for CCMs with different bending angles using a GA. The CCM consists of a 40×6 subarray with a total length of 400 mm, corresponding to the ROC are [254.65, 190.99, 152.78 mm], with central angles of central angles $[90°, 120°, 150°]$, respectively. To analyze the effect of subarray layout on scattering manipulation, we first simulated the scattering performances of the conformal structure without any I-shaped GAF patterns. As shown in Fig. 7, because of the attachment of a large continuous GAF layer at the bottom, the conformal structure can be approximated as a cylindrical

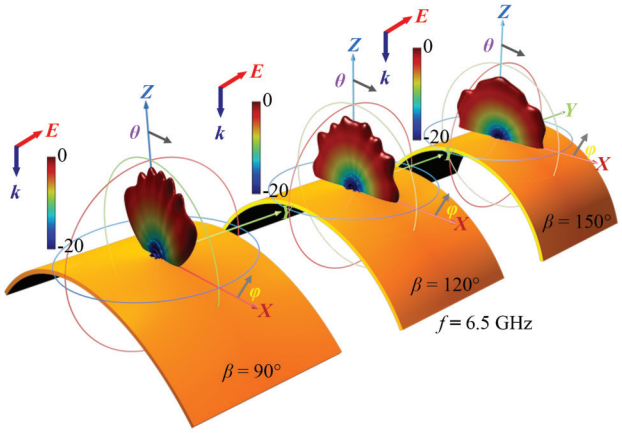

Fig. 7. Scattering performances of the conformal structure without any I-shaped GAF patterns.

conductor. For a normally incident TE-polarized wave at a frequency of 6.5 GHz, the behavior of the scattered waves on the conformal surface mainly consists of specular reflection, creeping waves, and diffraction effects [54]. At $\beta = 90°$, the surface curvature is relatively moderate. Specular reflection plays a dominant role, and the backscattered waves are mainly concentrated in the vertical direction. As β increases from 90° to 150°, the reduction of ROC enhances the energy of the creeping and diffracted waves, causing more incident waves to propagate along the conformal surface. Because of the discontinuity at the edges of the conformal surface, the creeping and diffracted waves propagate in different directions at the end of the structure. Consequently, the distribution of scattered waves gradually expands, and the backscattered fields are not only concentrated in the vertical direction but also distributed over a wider angle range. The control of these surface waves can be analyzed using the surface impedance theory [55], which is beyond the scope of this work.

We pay more attention to the precise control of the main scattered beam using the proposed CAST method. Fig. 8(a)–(c) shows the simulated 3-D far-field scattering patterns of different CCMs at 6.5 GHz, where colored blocks are used to represent the coding state of the subarrays. For CCMs with three distinct central angles [90°, 120°, 150°], the scattered waves are anomalously redirected into a primary direction in the *xoz* plane, with reflection angles [35°, 30°, 25°], respectively. As shown in Fig. 8(d), the predicted single-beam profiles from CAST and simulations are in good agreement. This indicates that most of the available scattering energy is allocated to the intended primary direction. However, the specular reflection and surface wave effects cause the simulation sidelobe to deviate from the results calculated by CAST. Another coding strategy is employed to achieve double-beam generation, as shown in Fig. 8(e)–(g). Based on spatial symmetry, the optimized data are reduced to a quarter, forming a symmetric coding matrix in all directions. The scattered waves are anomalously redirected in two directions in the *xoz* plane, the reflection angles being [±25°, ±30°, ±35°]. As shown in Fig. 8(h), the predicted double-beam profiles from CAST. The simulated results are consistent. More sidelobes are concentrated in the vertical and lateral directions as a result of specular reflection and surface wave effects.

C. Curvature-Based Dynamic Single-Beam Scanning

The CCM based on the flexible GAF can provide additional spatial freedom through structural bending. According to (12), the far-field scattering pattern $F(\theta, \varphi)$ is closely related to the position of the subarray $\theta_{(n)}$. When a layout of the subarray is determined, combined with (5), variations in the central angle β can change the direction of the scattered beam. When a CCM bends at three different center angles $[\beta_1, \beta_2, \beta_3]$, the expected main beam directions can be denoted as $[\theta_1, \theta_2, \theta_3]$ in the $\varphi = 0°$ plane. The optimized objective function (20) can be rewritten as

$$\begin{aligned} Fitness\,(g, \beta_1, \beta_2, \beta_3) = {} & W_1 \cdot Fitness\,(g, \beta_1) \\ & + W_2 \cdot Fitness\,(g, \beta_2) \\ & + W_3 \cdot Fitness\,(g, \beta_3) \end{aligned} \tag{21}$$

where the weighting coefficients W_1, W_2, W_3 are set to 1, 1.05, and 1, respectively. As shown in Fig. 9, the optimized coding sequence [10101010110100111000...] is encoded on the conformal structure. The CCM with different curvatures are labeled as $[a_1, a_2, a_3]$, corresponding to the central angle $[\beta_1 = 90°, \beta_2 = 100°, \beta_3 = 110°]$. As indicated by the red arrow, the main beam direction is related to β, which are $[\theta_1 = 26°, \theta_2 = 31°, \theta_3 = 34°]$. Therefore, the change range of the center angle is $\Delta\beta = 20°$, and the angle of deflection of the single-beam is $\Delta\theta = 8°$ as β increases. Fig. 10(a) illustrates the simulated 2-D normalized far-field scattering patterns of the CCM in the $\varphi = 0°$ plane for different central angles β. At a frequency of 6.5 GHz, as β changes from 90° to 110°, the direction of the single-beam shifts toward a larger angle. In addition, we extend the range of β in the inset. The maximum angle of deflection of the main beam is $\Delta\theta = 14°$, when β varies from 80° to 120°. It can be seen that the main beam direction θ and β are not a linear relationship, but rather increases in discrete steps, forming a staircase-like curve. In the operating bandwidth (6.2–6.8 GHz), according to (12), the beam angle θ is determined by both the central angle β and the frequency f. As shown in Fig. 10(b), for any given f, different color regions represent the discrete intervals at which θ adjusts as β increases, consistent with the simulated results. When β remains constant, the change in θ with f is negligible. The main beam direction deviation remains within 2°, indicating that the scattered beam of the CCM exhibits angular stability in the operating frequency band.

In summary, the precise prediction of the beam and reliable optimization results are attributed to the proposed CAST method. For any intelligent optimization algorithm, the required optimization procedure can be established based on CAST. In this article, the objective function used in GA-based optimization is directly derived from the theoretical predictions provided by CAST. This close integration means that any inaccuracies in the CAST would directly impact the convergence behavior and the reliability of the optimized coding

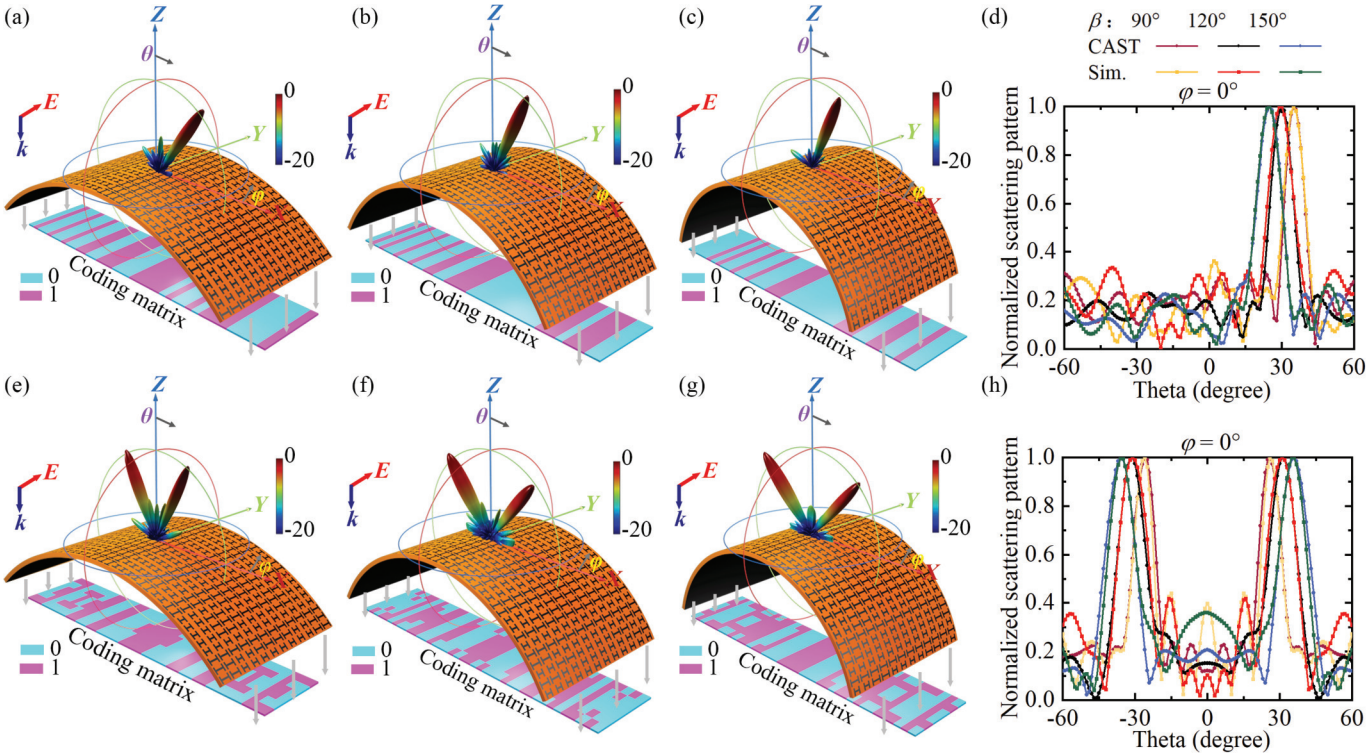

Fig. 8. Simulated 3-D far-field scattering patterns of different CCMs. (a)–(c) Single-beam generation. (e)–(g) Double-beam generation. (d) and (h) Results from CAST and simulations (Sim.).

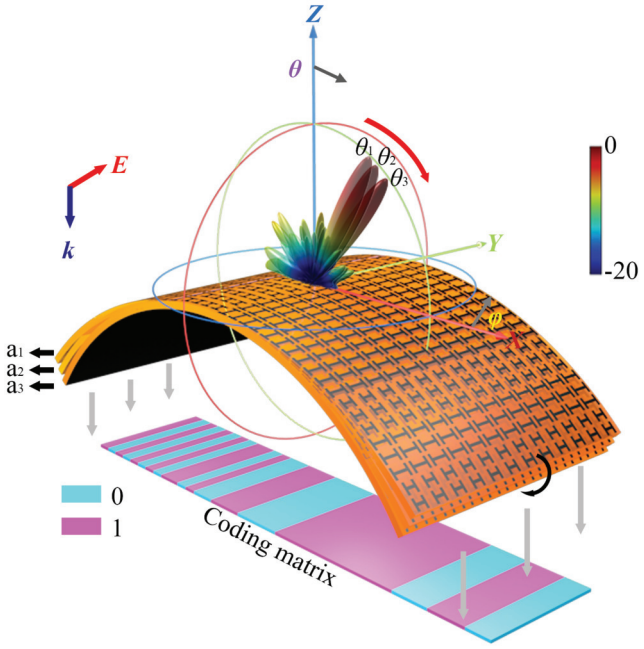

Fig. 9. Manipulation of the scattered beam through structural bending.

matrix. To further demonstrate the accuracy and significance of CAST in beam prediction and optimization, we compare the results between CAST, PSM, and simulations. Fig. 10(c)–(e) shows the normalized scattering patterns in the *uv* plane for the CCMs with different curvatures $[a_1, a_2, a_3]$. Here, the far-field scattering pattern of the CCM computed by PSM can be written as

$$F_{\mathrm{P}}(\theta,\varphi)=\sum_{m=1}^{M}\sum_{n=1}^{N}\exp\left\{-\mathrm{j}\left[\phi'_{(m,n)}+\phi_{(m,n)}\left(\theta_{(n)},f\right)\right]\right\} \tag{22}$$

where the term $\phi_{l_{(n)}}$ related to $P^{\theta_{(n)}}(\theta,\varphi)$ has been removed. In (22), the scattering contribution of the subarray in space has been regarded as isotropic, equal to the value one. Instead, CAST considers the variations in the scattering shadow regions of subarrays with different spatial positions. Combined with Fig. 9, according to the coding matrix, the left part of the CCM has a distinct phase gradient, which directs the scattered energy toward the right hemispherical space. Meanwhile, the left subarrays contribute minimally to the scattering intensity near the spatial edge of the right hemisphere. As shown in Fig. 10(c), the simulated main beam contour (white solid line) shifts rightward as the CCM curvature increases. However, the scattering intensity in the region near u = 1 (red solid line) remains relatively low due to the accumulation of scattering shadows from each subarray. In Fig. 10(d), the CAST accurately represents the main beam contour closely matching the simulation at different curvatures. Furthermore, CAST precisely calculates the scattering shadow (red solid line), demonstrating its robustness in predicting the reduced scattering intensity in this region. In contrast, as depicted in Fig. 10(e), the PSM results exhibit a significantly distorted beam contour and an inaccurate scattering shadow, particularly at higher curvatures a_3. Specifically, as the CCM curvature increases from a_1 to a_3, the scattering field calculated by PSM significantly intensifies near the u = 1 region, with more

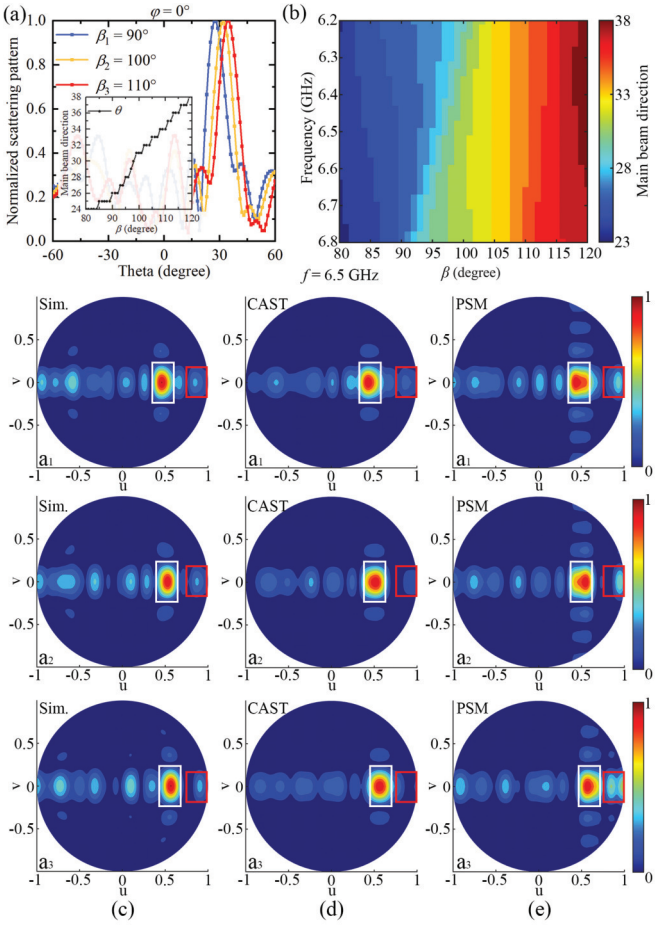

Fig. 10. (a) 2-D normalized far-field scattering patterns of the CCMs with varying central angles β. The inset illustrates the variation in the main beam direction θ as β increases from 80° to 120°. (b) Relationship between θ and β within the frequency range of 6.2–6.8 GHz. (c)–(e) Normalized scattering patterns of the CCMs with different curvatures $[a_1, a_2, a_3]$ in the uv plane, with results obtained through Sim., CAST, and PSM, respectively. The main beam contour is marked by the white solid line, while the red solid line highlights the scattering shadow region ($u = \sin\theta\cos\varphi$, $v = \sin\theta\sin\varphi$).

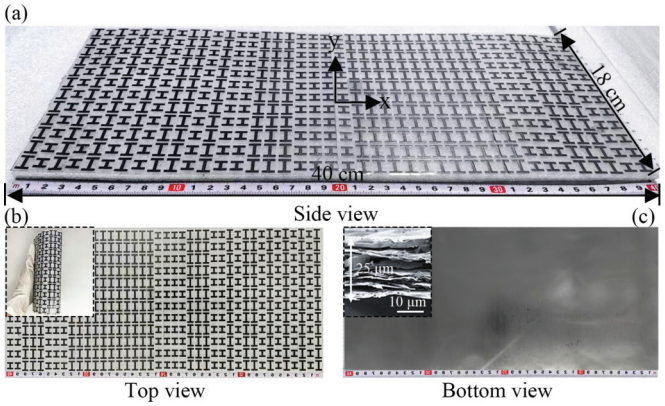

Fig. 11. (a) Side view of the prototype. (b) Top view of the prototype, with the inset illustrating the curl status. (c) Bottom view of the prototype, with the inset showing the cross-sectional SEM image of the GAF.

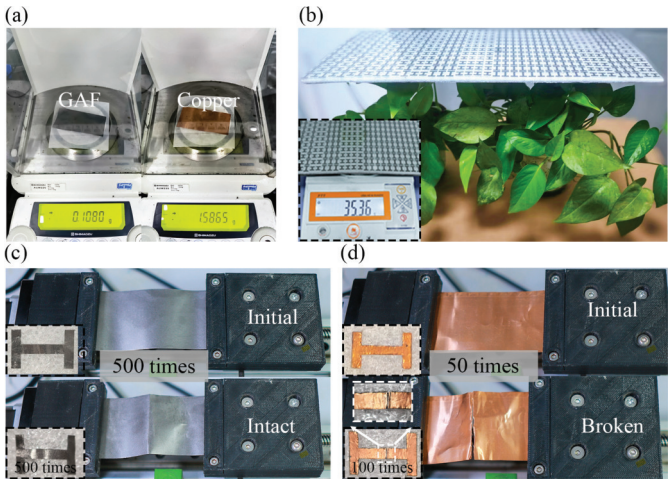

Fig. 12. (a) Mass of the GAF with a thickness of 25 μm compared to copper with a thickness of 67 μm. (b) CCM placed horizontally above plant leaves, with the inset illustrating the total mass of the CCM. (c) and (d) Comparison of bending times between the GAF and copper foil. The insets illustrate the bending tests of metasurface structures made from the GAF and copper foil.

scattering patterns appearing along the v-direction, resulting in more unwanted sidelobes. Assuming that both methods are involved in the layout optimization of CCMs, because the CAST results are more accurate and closely align with the simulations, making the optimized coding matrix more trustworthy and significantly enhancing optimization efficiency. In contrast, the PSM results exhibit beam distortion and additional scattering regions; even if the derived coding matrix is utilizable, these discrepancies often lead to it being overlooked and abandoned, ultimately reducing the overall optimization efficiency. Therefore, it is meaningful to account for the scattering shadow regions in the CAPS. The proposed CAST method is more reliable than the PSM method in computing and optimizing the scattering fields of CCMs.

IV. Experimental Verification

To validate the theory and design, the proposed CCM is fabricated and measured. Fig. 11(a) presents a side view of the fabricated prototype, the I-shaped GAF pattern is etched onto a PET medium with a thickness of 50 μm using the laser engraver (LPKF ProtoLaser S). The complete prototype consists of 40×12 elements, corresponding to 40×6 subarrays, with an overall size of 40×18 cm. The pattern film is then transferred to the surface of the EPE foam using an optically clear adhesive (OCA). Fig. 11(b) and (c) shows the top and bottom views of the prototype, respectively, with the insets illustrating the curl status of the prototype and a cross-sectional SEM image of the GAF. Unlike the dense atomic structure of metallic materials, the GAF consists of multiple layers of graphene nanosheets, and the interlayer spacing influences EM response. As the frequency increases to the terahertz bands, the EM absorption properties of the GAF become more pronounced, which is beneficial to EM shielding [56]. For microwave frequencies, the EM performance of the GAF is almost indistinguishable from that of copper, while offering significant advantages in terms of flexibility and weight reduction.

As shown in Fig. 12(a), the mass of the GAF and copper foil with an area of 40×80 mm is measured to be 0.108

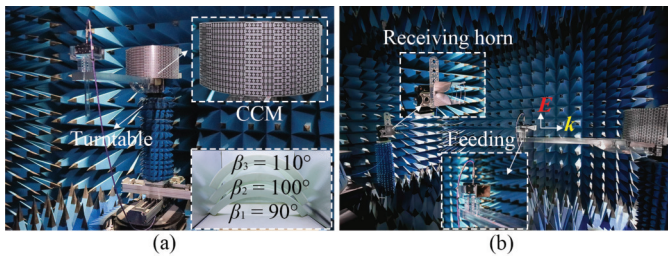

Fig. 13. (a) Prototype combined 3-D-printed arc-shaped structures. (b) Enlarged view of the feed and receiving antenna in an anechoic chamber.

and 1.5865 g, respectively. The thicknesses of the GAF and copper are 25 and 67 μm, respectively. Therefore, the density of the GAF is 1.46 g/cm^3, which is only 17% of that of the copper foil (8.6 g/cm^3). Fig. 12(b) shows that the CCM, with a mass of 35.36 g, can be positioned horizontally on top of the plant leaves without exerting a noticeable downward force. Importantly, the GAF exhibits superior mechanical properties compared to copper. The fatigue resistance of the GAF is tested as shown in Fig. 12(c). After 500 bending cycles, the GAF remained almost unchanged and intact. In contrast, Fig. 12(d) shows that the copper foil exhibited clear signs of breakage after 50 bending cycles due to metal fatigue. Additionally, the insets illustrate bending tests of elements, where I-shaped structures of the GAF and copper foil are attached to flexible foam substrates. After 500 bending cycles, the surface of the GAF I-shaped structure remained smooth and intact; correspondingly, after only 100 bending cycles, the copper I-shaped structure exhibited noticeable wrinkles and damage. These results confirm the reliability of the GAF in flexible metasurface designs. As a result, the GAF-based CCMs can have adjustable curvature and bending resistance. To verify the impact of curvature on scattering beam control, the measured environments for experiment are shown in Fig. 13(a). In this configuration, the CCM is positioned on a turntable equipped with a horizontal slide rail and an arc-shaped structure is behind it. In the inset, the arc-shaped structures are 3-D printed from resin material with center angles of $[90°, 100°, 110°]$. As shown in Fig. 13(b), a 6–18-GHz linearly polarized horn placed at the center of the receiving side of the CCM is used as a feeding, while a 1–20-GHz broadband horn antenna serves as a receiving part. The inset provides an enlarged view of the horn antenna, where the feed is placed 80 cm from the CCM to simulate the incidence of normal plane waves. By automatically rotating the turntable, the scattering power at all angles is received by the broadband horn antenna and recorded using a vector network analyzer.

Fig. 14(a) presents the simulated and measured results of the CCM with different center angles at 6.5 GHz. For the center angles $[\beta_1 = 90°, \beta_2 = 100°, \beta_3 = 110°]$, the measured peak of the CCM occur at $\theta_{e1} = 25°$, $\theta_{e2} = 31°$, and $\theta_{e3} = 35°$, respectively, differing from the simulated results by $-1°$, $0°$, and $1°$, respectively. The maximum angle of deflection of the main beam is $\Delta\theta = 10°$, when β changes by $20°$. Therefore, dynamic beam scanning based on curvature can be realized. The variation of the main beam (highlighted in the gray area) is broadly consistent between the simulated and measured

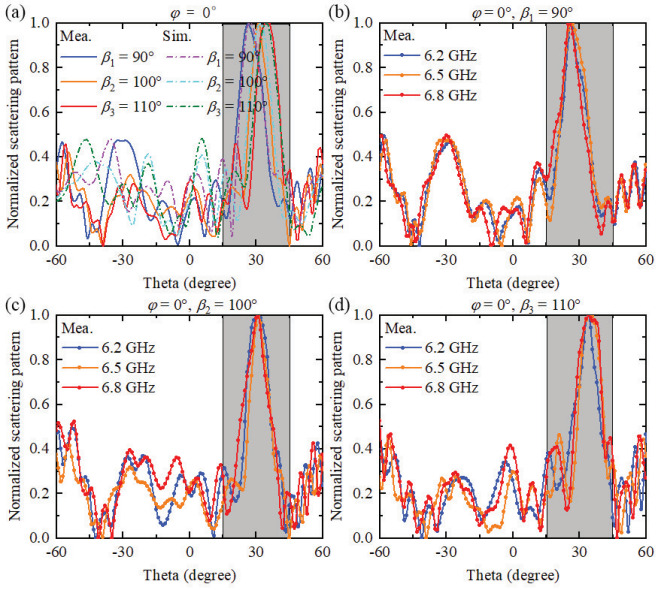

Fig. 14. (a) Sim. and measured (Mea.) results of the CCM with different center angles. (b)–(d) Mea. results of the CCM with different center angles for three frequency points.

results, while some small discrepancies are observed in the sidelobe regions. These deviations are commonly observed in practical measurements and can be influenced by slight imperfections in the fabrication process, such as misalignment, patterning errors, or surface roughness. Additionally, the horn antenna used for excitation produces a spherical wavefront, whose amplitude and phase distribution differ from those of an ideal plane wave. This discrepancy in wavefront shape may further affect the sidelobe positions in the measurements. Despite these small discrepancies, the measured mainlobes and overall scattering distributions closely match the simulations. For other operating frequencies [6.2, 6.5, 6.8 GHz], as shown in Fig. 14(b)–(d). When β is determined, the measured peaks for the three frequencies nearly coincide at the same deflection angles, remaining close to $[25°, 31°, 35°]$, respectively. This is consistent with the results obtained using the CAST method [as shown in Fig. 10(b)]. Therefore, the measured results confirm the reliability of the CAST method, which is valuable for both flexible and conformal platforms.

V. Conclusion

In this article, we propose a novel methodology, CAST, to overcome the challenge of scattering shadow regions in conformal arrays. Building on CAST, we develop an optimization algorithm for CCMs. For CCMs with central angles of $[90°, 120°, 150°]$, the reflection angles for the single beam are $[35°, 30°, 25°]$, while for the double beam, the reflection angles are $[\pm 25°, \pm 30°, \pm 35°]$. In particular, the simulation results for the main beam profiles are in good agreement with the predictions made by CAST. Additionally, the flexible GAF enhances the adaptability of CCMs, allowing beam scanning through adjustable curvature. Finally, a prototype is fabricated and experimentally measured to validate the reliability of the CAST. For CCMs with center angles

$[\beta_1 = 90°, \beta_2 = 100°, \beta_3 = 110°]$, the measured reflection angles are $[25°, 31°, 35°]$, with a deviation of $\pm 1°$ from the simulation. These results demonstrate that CAST can accurately predict both the direction and profile of the beam. Furthermore, mechanical tests confirm that the GAF-based CCM is flexible and lightweight, making it suitable for applications on curved platforms. This approach offers a novel strategy for wavefront manipulation on curved surfaces, such as aircraft and vehicles, and facilitates the design of conformal arrays for various aerodynamic profiles.

REFERENCES

[1] L. Bao et al., "Design of digital coding metasurfaces with independent controls of phase and amplitude responses," *Appl. Phys. Lett.*, vol. 113, no. 6, Aug. 2018, Art. no. 063502.

[2] L. Bao et al., "Multi-beam forming and controls by metasurface with phase and amplitude modulations," *IEEE Trans. Antennas Propag.*, vol. 67, no. 10, pp. 6680–6685, Oct. 2019.

[3] Q. Lou and Z. N. Chen, "Sidelobe suppression of metalens antenna by amplitude and phase controllable metasurfaces," *IEEE Trans. Antennas Propag.*, vol. 69, no. 10, pp. 6977–6981, Oct. 2021.

[4] Y. Huang et al., "Catenary electromagnetics for ultra-broadband lightweight absorbers and large-scale flat antennas," *Adv. Sci.*, vol. 6, no. 7, Apr. 2019, Art. no. 1801691.

[5] H.-R. Zu et al., "Optically and radiofrequency-transparent metadevices based on quasi-one-dimensional surface plasmon polariton structures," *Nature Electron.*, vol. 6, no. 7, pp. 525–533, Jul. 2023.

[6] N. K. Grady et al., "Terahertz metamaterials for linear polarization conversion and anomalous refraction," *Science*, vol. 340, no. 6138, pp. 1304–1307, Jun. 2013.

[7] X. Huang, D. Yang, and H. Yang, "Multiple-band reflective polarization converter using U-shaped metamaterial," *J. Appl. Phys.*, vol. 115, no. 10, Mar. 2014, Art. no. 103505.

[8] M. I. Khan, B. Hu, Y. Chen, N. Ullah, M. J. I. Khan, and A. R. Khalid, "Multiband efficient asymmetric transmission with polarization conversion using chiral metasurface," *IEEE Antennas Wireless Propag. Lett.*, vol. 19, no. 7, pp. 1137–1141, Jul. 2020.

[9] J. Liu, J.-Y. Li, and S.-G. Zhou, "Polarization conversion metamaterial surface with staggered-arrangement structure for broadband radar cross section reduction," *IEEE Antennas Wireless Propag. Lett.*, vol. 18, no. 5, pp. 871–875, May 2019.

[10] C. Huang, W. Pan, X. Ma, and X. Luo, "Wideband radar cross-section reduction of a stacked patch array antenna using metasurface," *IEEE Antennas Wireless Propag. Lett.*, vol. 14, pp. 1369–1372, 2015.

[11] A. Y. Modi, M. A. Alyahya, C. A. Balanis, and C. R. Birtcher, "Metasurface-based method for broadband RCS reduction of dihedral corner reflectors with multiple bounces," *IEEE Trans. Antennas Propag.*, vol. 68, no. 3, pp. 1436–1447, Mar. 2020.

[12] W. Cai, U. K. Chettiar, A. V. Kildishev, and V. M. Shalaev, "Optical cloaking with metamaterials," *Nature Photon.*, vol. 1, no. 4, pp. 224–227, Apr. 2007.

[13] D. Schurig et al., "Metamaterial electromagnetic cloak at microwave frequencies," *Science*, vol. 314, no. 5801, pp. 977–980, Nov. 2006.

[14] N. Yu et al., "Light propagation with phase discontinuities: Generalized laws of reflection and refraction," *Science*, vol. 334, no. 6054, pp. 333–337, Oct. 2011.

[15] T. J. Cui, M. Q. Qi, X. Wan, J. Zhao, and Q. Cheng, "Coding metamaterials, digital metamaterials and programmable metamaterials," *Light, Sci. Appl.*, vol. 3, no. 10, p. e218, Oct. 2014.

[16] N. Zhang et al., "Programmable coding metasurface for dual-band independent real-time beam control," *IEEE J. Emerg. Sel. Topics Circuits Syst.*, vol. 10, no. 1, pp. 20–28, Mar. 2020.

[17] C. Huang et al., "Reconfigurable metasurface cloak for dynamical electromagnetic illusions," *ACS Photon.*, vol. 5, no. 5, pp. 1718–1725, May 2018.

[18] H. Lin et al., "A dual-band reconfigurable intelligent metasurface with beam steering," *J. Phys. D, Appl. Phys.*, vol. 55, no. 24, Jun. 2022, Art. no. 245002.

[19] M. Kim, J. Jeong, J. K. S. Poon, and G. V. Eleftheriades, "Vanadium-dioxide-assisted digital optical metasurfaces for dynamic wavefront engineering," *J. Opt. Soc. Amer. B, Opt. Phys.*, vol. 33, no. 5, pp. 980–988, 2016.

[20] C. H. Chu et al., "Active dielectric metasurface based on phase-change medium," *Laser Photon. Rev.*, vol. 10, no. 6, pp. 986–994, Nov. 2016.

[21] Q. Wang et al., "Optically reconfigurable metasurfaces and photonic devices based on phase change materials," *Nature Photon.*, vol. 10, no. 1, pp. 60–65, Jan. 2016.

[22] S. Walia et al., "Flexible metasurfaces and metamaterials: A review of materials and fabrication processes at micro- and nano-scales," *Appl. Phys. Rev.*, vol. 2, no. 1, Mar. 2015, Art. no. 011303.

[23] K. Wu, P. Coquet, Q. J. Wang, and P. Genevet, "Modelling of free-form conformal metasurfaces," *Nature Commun.*, vol. 9, no. 1, p. 3494, Aug. 2018.

[24] K. Rouhi, H. Rajabalipanah, and A. Abdolali, "Real-time and broadband terahertz wave scattering manipulation via polarization-insensitive conformal graphene-based coding metasurfaces," *Annalen der Physik*, vol. 530, no. 4, Apr. 2018, Art. no. 1700310.

[25] P.-Y. Chen, J. Soric, Y. R. Padooru, H. M. Bernety, A. B. Yakovlev, and A. Alù, "Nanostructured graphene metasurface for tunable terahertz cloaking," *New J. Phys.*, vol. 15, no. 12, Dec. 2013, Art. no. 123029.

[26] L. Liang, "Anomalous terahertz reflection and scattering by flexible and conformal coding metamaterials," *Adv. Opt. Mater.*, vol. 3, no. 10, pp. 1374–1380, 2015.

[27] C. Fan, W. Zhao, K. Chen, J. Zhao, T. Jiang, and Y. Feng, "Optically transparent conformal reflectarray with multi-angle microwave efficient scattering enhancement," *Adv. Opt. Mater.*, vol. 12, no. 18, Jun. 2024, Art. no. 2400151.

[28] H. Li, G.-M. Wang, G. Hu, T. Cai, C.-W. Qiu, and H.-X. Xu, "3D-printed curved metasurface with multifunctional wavefronts," *Adv. Opt. Mater.*, vol. 8, no. 15, Aug. 2020, Art. no. 2000129.

[29] Y. Zhou et al., "Wavefront control of 2D curved coding metasurfaces based on extended array theory," *IEEE Access*, vol. 7, pp. 158427–158433, 2019.

[30] Y. Wang, J. Su, Z. Li, Q. Guo, and J. Song, "A prismatic conformal metasurface for radar cross-sectional reduction," *IEEE Antennas Wireless Propag. Lett.*, vol. 19, pp. 631–635, 2020.

[31] A. B. Petrin, "Electromagnetic wave propagation from a point source in air through a medium with a negative refractive index," *JETP Lett.*, vol. 87, no. 9, pp. 464–469, Jul. 2008.

[32] C. Athanasiadis, P. A. Martin, A. Spyropoulos, and I. G. Stratis, "Scattering relations for point sources: Acoustic and electromagnetic waves," *J. Math. Phys.*, vol. 43, no. 11, pp. 5683–5697, Nov. 2002.

[33] Y. Zhou et al., "Design of phase gradient coding metasurfaces for broadband wave modulating," *Sci. Rep.*, vol. 8, no. 1, p. 8672, 2018.

[34] M. A. S. M. Al-Haddad, N. Jamel, and A. N. Nordin, "Flexible antenna: A review of design, materials, fabrication, and applications," *J. Phys., Conf. Ser.*, vol. 1878, no. 1, May 2021, Art. no. 012068.

[35] X. Liu, Z. Yan, E. Wang, X. Zhao, T. Zhang, and F. Fan, "Multibeam forming with arbitrary radiation power ratios based on a conformal amplitude–phase-controlled metasurface," *IEEE Trans. Antennas Propag.*, vol. 71, no. 4, pp. 3707–3712, Apr. 2023.

[36] X.-Y. Luo et al., "Active cylindrical metasurface with spatial reconfigurability for tunable backward scattering reduction," *IEEE Trans. Antennas Propag.*, vol. 69, no. 6, pp. 3332–3340, Jun. 2021.

[37] D. Ye et al., "Flexible and compact tri-band graphene antenna for conformal Wi-Fi/WiMAX/5G applications," *IEEE Trans. Circuits Syst. II, Exp. Briefs*, vol. 71, no. 3, pp. 1086–1090, Mar. 2024.

[38] R. Song, R. Zhang, H. Zu, and D. He, "Graphene assembled films for radio frequency and microwave technology," *Accounts Mater. Res.*, vol. 5, no. 8, pp. 896–906, Aug. 2024.

[39] Y. Xin et al., "Millimeter-wave and short-range wireless communication antenna based on high-conductivity graphene-assembled film," *ACS Appl. Mater. Interface*, vol. 15, no. 47, pp. 54766–54772, Nov. 2023.

[40] L. Li et al., "Large-scale current collectors for regulating heat transfer and enhancing battery safety," *Nature Chem. Eng.*, vol. 1, no. 8, pp. 542–551, Aug. 2024.

[41] B. Zhang {et al.}, "Flexible anti-metal RFID tag antenna based on high-conductivity graphene assembly film," *Sensors*, vol. 21, p. 1513, Feb. 2021.

[42] W. Zhou et al., "Flexible radiofrequency filters based on highly conductive graphene assembly films," *Appl. Phys. Lett.*, vol. 114, no. 11, Mar. 2019, Art. no. 113503.

[43] R. Song et al., "Ultra-high conductive graphene assembled film for millimeter wave electromagnetic protection," *Sci. Bull.*, vol. 67, no. 11, pp. 1122–1125, Jun. 2022.

[44] H. R. Zu, B. Wu, Y. H. Zhang, Y. T. Zhao, R. G. Song, and D. P. He, "Circularly polarized wearable antenna with low profile and low specific absorption rate using highly conductive graphene film," *IEEE Antennas Wireless Propag. Lett.*, vol. 19, no. 12, pp. 2354–2358, Dec. 2020.

[45] L. Jiang, S. Yu, and N. Kou, "Asymmetric transmission of OAM vortex waves by cylindrical Janus metasurface," *IEEE Antennas Wireless Propag. Lett.*, vol. 22, pp. 2654–2658, 2023.
[46] M. Li et al., "Origami metawall: Mechanically controlled absorption and deflection of light," *Adv. Sci.*, vol. 6, no. 23, Dec. 2019, Art. no. 1901434.
[47] Y. Kato, K. Yonemura, K. Seki, R. Kambara, and A. Sanada, "Reconfigurable anomalous reflectors with stretchable elastic substrates at 140 GHz band," *Nanophotonics*, vol. 12, no. 13, pp. 2527–2535, Jun. 2023.
[48] M. Yazdi and M. Albooyeh, "Analysis of metasurfaces at oblique incidence," *IEEE Trans. Antennas Propag.*, vol. 65, no. 5, pp. 2397–2404, May 2017.
[49] H. Shi et al., "Gradient metasurface with both polarization-controlled directional surface wave coupling and anomalous reflection," *IEEE Antennas Wireless Propag. Lett.*, vol. 14, pp. 104–107, 2015.
[50] X. Luo, "Principles of electromagnetic waves in metasurfaces," *Sci. China Phys., Mech. Astron.*, vol. 58, no. 9, Sep. 2015, Art. no. 594201.
[51] T. Shan, X. Pan, M. Li, S. Xu, and F. Yang, "Coding programmable metasurfaces based on deep learning techniques," *IEEE J. Emerg. Sel. Topics Circuits Syst.*, vol. 10, no. 1, pp. 114–125, Mar. 2020.
[52] J. Robinson and Y. Rahmat-Samii, "Particle swarm optimization in electromagnetics," *IEEE Trans. Antennas Propag.*, vol. 52, no. 2, pp. 397–407, Feb. 2004.
[53] S. Yang, W. Lyu, B. Ning, Z. Zhang, and C. Yuen, "Flexible precoding for multi-user movable antenna communications," *IEEE Wireless Commun. Lett.*, vol. 13, no. 5, pp. 1404–1408, May 2024.
[54] A. Díaz-Rubio, V. S. Asadchy, A. Elsakka, and S. A. Tretyakov, "From the generalized reflection law to the realization of perfect anomalous reflectors," *Sci. Adv.*, vol. 3, no. 8, Aug. 2017, Art. no. 1602714.
[55] S. Pandi, C. A. Balanis, and C. R. Birtcher, "Design of scalar impedance holographic metasurfaces for antenna beam formation with desired polarization," *IEEE Trans. Antennas Propag.*, vol. 63, no. 7, pp. 3016–3024, Jul. 2015.
[56] R. Song et al., "Comparison of copper and graphene-assembled films in 5G wireless communication and THz electromagnetic-interference shielding," *Proc. Nat. Acad. Sci. USA*, vol. 120, no. 9, Feb. 2023, Art. no. 2209807120.

Zhi-Feng Li was born in Pingdingshan, Henan, China. He received the M.S. degree from the Central China Normal University (CCNU), Wuhan, China, in 2023. He is currently pursuing the Ph.D. degree in physics with Wuhan University of Technology (WUT), Wuhan.

His current research interests include conformal metasurfaces, graphene-based reflect arrays, and graphene-based heat dissipation technology.

Rong-Guo Song (Member, IEEE) is currently a special-term Professor with the School of Physics and Mechanics, Wuhan University of Technology, and Hubei Engineering Research Center of RF-Microwave Technology and Application. From 2022 to 2024, he was a Post-Doctoral with Air Force Early Warning Academy. During this period, he was seconded to the Qianyuan National Laboratory for one year. His research interests include graphene assembled film and microwave devices.

Hao-Ran Zu (Member, IEEE) was born in Xuzhou, Jiangsu Province, China, in 1994. He received the Ph.D. degrees in electromagnetic fields and microwave technology from Xidian University, Xi'an, China, in 2022.

Since 2023, he has worked at the School of Information Engineering, Wuhan University of Technology, and is currently a special-term Professor and the Ph.D. Supervisor with Hubei Engineering Research Center of RF-Microwave Technology and Application, Wuhan University of Technology. His research interests include antenna design and microwave devices based on metamaterials and metasurface.

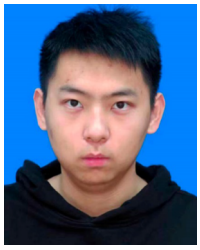

Yu Zhou was born in Tongling, Anhui, China, in 1998. He received the B.S. degree from Ningbo University, Zhejiang, China, in 2020. He is currently pursuing the Ph.D. degree with the School of Materials Science and Engineering, Wuhan University of Technology, Wuhan, China.

His research interests include graphene-based electromagnetic metasurfaces.

Yi-Tong Xin was born in Linyi, Shandong, China. He received the M.S. degree in physics from Wuhan University of Technology (WUT), Wuhan, China, in 2024, where he is currently pursuing the Ph.D. degree in electronic and information engineering.

His current research interests include base station antenna arrays, shared-aperture antennas, and decoupling technology.

Jian-Nan Guo was born in Changzhou, Jiangsu, China. He received the M.S. degree in physics from Wuhan University of Technology (WUT), Wuhan, China, in 2024, where he is currently pursuing the Ph.D. degree in radio physics.

His current research interests include dielectric transmitarray and reflectarray antennas and millimeter-wave antenna arrays.

Rui-Xue Zhang was born in Yantai, Shandong, China, in November 1996. She received the B.S. degree in electronic information science and technology from Wuhan University of Technology, Wuhan, China, in 2020, where she is currently pursuing the Ph.D. degree in radio physics.

Her current research interests include antenna design and microwave devices based on spoof surface plasmon polaritons.

Da-Ping He received the Ph.D. degree in materials processing engineering from Wuhan University of Technology, Wuhan, China, in 2013.

He is a Full Professor with Wuhan University of Technology. He was a Post-Doctoral with the University of Science and Technology of China, Hefei, China, and subsequently joined the University of Bath, Bath, U.K., as a Newton International Fellow and the University of Cambridge, Cambridge, U.K., as a Post-Doctoral. His research focuses on the preparation and application of nanocomposite materials for new energy devices, sensors, and RF/microwave technologies.